

Electron Transfer in Rhodamine–TiO₂ Complexes Studied as a Function of Chalcogen and Bridge Substitution

Zachary Piontkowski, Yu-Chen Wang, Yu-Xiu Liu, Yi Zhao, and David W. McCamant*

Cite This: *J. Phys. Chem. C* 2020, 124, 2851–2863

Read Online

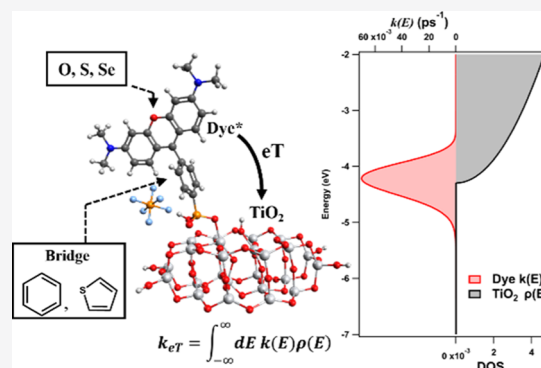
ACCESS |

Metrics & More

Article Recommendations

Supporting Information

ABSTRACT: Many emerging light-harvesting systems for solar-energy capture depend on absorption of light by molecular dyes and subsequent electron transfer to metal-oxide semiconductors. However, the inhomogeneous electron-transfer process is often misunderstood when analogies from bimolecular electron transfer are used to explain experimental trends. Here, we develop and apply a theoretical methodology that correctly incorporates the semiconductor density of states and the system reorganization energies to explain observed trends in a series of molecular sensitizers. The effects of chalcogen and bridge substitution on the electron transfer in rhodamine–TiO₂ complexes are theoretically investigated by combining density functional theory (DFT)/time-dependent DFT calculations and Fermi's golden rule for the rate constant. It is shown that all dyes exhibit $\tau_{eT} < 4$ ps. Dyes with thiophene bridges exhibit shorter τ_{eT} (~ 1 ps) than dyes with phenylene bridges (~ 4 ps). When the planes of the dye core and bridge are fixed at coplanarity, the dye–TiO₂ coupling strength is found to increase by a factor of ~ 2 when compared with the Franck–Condon geometry. However, the donor energy level of coplanar dyes falls significantly below the TiO₂ conduction band edge so that, despite enhanced coupling, electron transfer is slowed to ~ 20 ps. Similar results appear for the excited triplet states of these dyes, showing that the intersystem crossing to low energy triplet states can increase electron-transfer time constants to 60–240 ps. These results are compared to the results of previous photocatalytic hydrogen generation and dye-sensitized solar cell experiments.



INTRODUCTION

Previous studies have demonstrated the effectiveness of rhodamine dyes (Figure 1) as dye-sensitizers for photocatalytic hydrogen generation and dye-sensitized solar cells.^{1–5} However, there lacks a systematic comparison of the effect of different rhodamine analogues on electron-transfer rates and efficiency. Specifically, previous studies have suggested that “para”-substituted thiophene bridges will more strongly couple donor and acceptor moieties when compared with phenylene bridges.⁶ Thiophene derivatives are also known to undergo sub-10 ps nuclear reorganization to a π -delocalized coplanar geometry along the dihedral coordinate τ (Figure 1), which will result in greater orbital overlap with a semi-conductor acceptor.^{7,8} This is expected to result in faster electron transfer and therefore more efficient light-energy conversion. A direct comparison of the effect of different bridge structures on electron-transfer rates, however, is still lacking, preventing a definitive conclusion about the optimal bridge structure for rhodamine dyes. One possibility is that the lower energy of the coplanar geometry will reduce the driving force for electron transfer, effectively deactivating electron transfer, despite stronger coupling.

Another structural aspect to be investigated is the core chalcogen of the rhodamine dye. Previous results show that selenium-containing chromophores are most effective for

photocatalytic hydrogen generation, followed by sulfur and finally by oxygen.¹ This contrasts with photocurrent efficiencies, which show a negligible dependence on chalcogen substitution.^{2–5} The exceptional photocatalytic hydrogen generation achieved by selenium-substituted rhodamine derivatives was attributed to higher rates of intersystem crossing to a long-lived triplet state.¹ Because electron transfer was thought to be much slower than the singlet lifetime, the long-lived triplet state was described as vital for efficient hydrogen production.¹ However, because the lowest energy T₁ triplet states of organic chromophores generally fall below their singlet S₁ states, it is not clear whether the dye in the triplet state will have an oxidation potential which can support electron transfer to a TiO₂ conduction band. Furthermore, similar rhodamine–TiO₂ systems are known to undergo electron transfer in 1 to 300 ps, making the need for a microsecond lifetime triplet state unlikely.^{9,10} Overall, the role of the chalcogen needs to be reexamined.

Received: November 26, 2019

Revised: January 10, 2020

Published: January 10, 2020

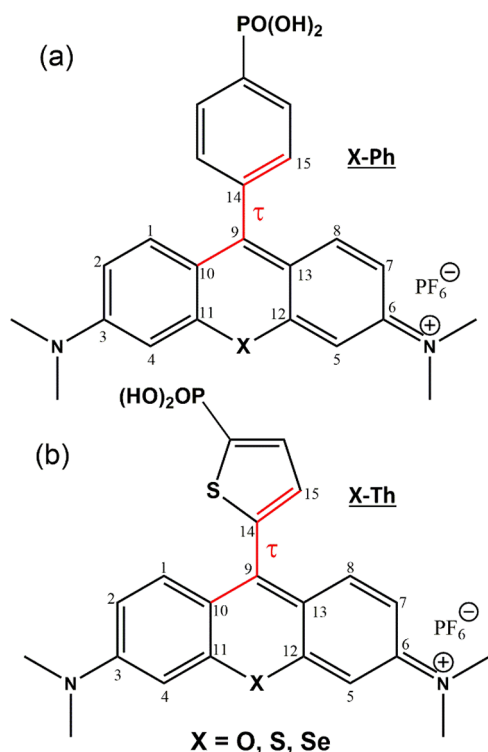


Figure 1. Rhodamine dye sensitizers with (a) phenylene or (b) thiophene bridges. The chalcogen in the center of the xanthilium core, labeled X, can be substituted with O, S, or Se.

In this work, we provide a computational picture of the rhodamine–TiO₂ electron-transfer process. We compare electronic coupling strength, free-energy gaps, reorganization energies, and electron-transfer rates between various rhodamine analogues for comparison to previous experimental results. We investigate the effect of dye coplanarity on electronic coupling strength and driving force to establish whether such reorganization events enhance or hinder the electron-transfer process. A model for electron transfer is presented which retains the full vibronic structure of the rhodamine–TiO₂ complexes while approximating the semiconductor conduction band with a functional form for the density of states. This theory retains the temperature dependence of electron transfer which becomes important when the occupied electron donor state is near or below the band edge of the semiconductor acceptor. This approach improves upon a simple Marcus theory electron-transfer picture where electron transfer is assumed to be thermally activated.^{11,12} It rather uses a time-domain Fermi's golden rule expression for electron transfer to enable an explicit description of the vibrational normal modes which couple to the electron-transfer process.^{10,13–17} The heterogeneous electron-transfer rate is expressed by introducing a semiconductor conduction band density of states to act as an acceptor. In a fashion similar to Gerischer^{18,19} and Sakata,¹⁰ the overlap between the vibronic distribution of the donor and acceptor (in this case the semiconductor density of states) accounts for the vibronic overlap between the redox states of donors and acceptors. The parameters required to compute electron transfer rates in this framework (electronic coupling strengths, reorganization energies and redox potentials) are computed using density functional electronic structure methods. Although limitations in the accuracy of calculations of semiconductor properties,

such as the flat-band potential, prevent definitive conclusions about the absolute time scale of electron transfer, these calculations are a way to internally compare between dyes. The similarities and differences between dyes are compared to previous results of dye-sensitized solar cells and photocatalytic H₂ generation experiments.

THEORY

Electron-Transfer Rate. For electron transfer in a donor–acceptor system, modeling ground, initial, and final states as diabatic states in the harmonic approximation, the following model Hamiltonian is considered

$$\begin{aligned}
 H = \hat{T} + & \left(\epsilon_g + \frac{1}{2} \sum_j \omega_j^2 \hat{Q}_j^2 \right) |DA\rangle \langle DA| \\
 & + \left(\epsilon_e + \frac{1}{2} \sum_j \omega_j^2 (\hat{Q}_j - Q_{j,e})^2 \right) |D^*A\rangle \langle D^*A| \\
 & + \left(\epsilon_{CT} + \frac{1}{2} \sum_j \omega_j^2 (\hat{Q}_j - Q_{j,CT})^2 \right) |D^+A^-\rangle \langle D^+A^-| \\
 & + V(|D^*A\rangle \langle D^+A^-| + |D^+A^-\rangle \langle D^*A|)
 \end{aligned} \quad (1)$$

Here, $|DA\rangle$, $|D^*A\rangle$, and $|D^+A^-\rangle$ are the electronic ground state, the local excited state, and the charge-transfer state with the corresponding energies ϵ_g , ϵ_e , and ϵ_{CT} , respectively. \hat{Q}_j represents the normal mode coordinate with frequency ω_j and originates from internal or solvent modes, and \hat{T} is the kinetic energy operator of these modes. $Q_{j,e}$ and $Q_{j,CT}$ are the nuclear shifts between $|DA\rangle$ and $|D^*A\rangle$ and between $|DA\rangle$ and $|D^+A^-\rangle$, respectively. V is the electronic coupling between $|D^*A\rangle$ and $|D^+A^-\rangle$.

The initial state for the electron transfer can be significantly distorted from the excited-state equilibrium geometry because of the shifts $Q_{j,e}$ between $|DA\rangle$ and $|D^*A\rangle$, which leads to transient excess vibrational excitation following the absorption event. However, if the electron transfer is much slower than the vibrational relaxation process, it is reasonable to assume an equilibrium initial state that is thermally equilibrated at the minimum of the potential energy surface of $|D^*A\rangle$ before electron transfer. Under this assumption and treating the electronic coupling as a perturbation, the rate constant can be expressed as

$$k_{eT} = \frac{2}{\hbar^2} |V|^2 \Re \int_0^\infty dt e^{-i/\hbar \Delta G t + L(t) + g(t)} \quad (2)$$

Here, \Re denotes to take the real part, and ΔG is the free-energy gap. $L(t)$ is a function that incorporates the influence from the electron–vibration interaction

$$L(t) = - \sum_j S_j [(2\bar{n}_j + 1)(1 - \cos \omega_j t) + i \sin \omega_j t] \quad (3)$$

where $S_j = \frac{1}{2\hbar} \mu_j \omega_j (Q_{j,e} - Q_{j,CT})^2$ is the dimensionless Huang–Rhys factor where μ_j is the reduced mass of normal mode j , and $\bar{n}_j = (e^{\hbar\omega_j/k_B T} - 1)^{-1}$ is the vibrational occupation number. $g(t)$ is a function incorporating interaction with the bath solvent. Equation 2 is the well-known Fermi's golden rule expression for the rate constant.^{16,17,20} The equilibrium assumption implied in eq 2 is valid for all dye–semiconductor complexes investigated in this work because the timescale of

vibrational relaxation from the Franck–Condon region (<100 fs) is much smaller than the timescale of electron-transfer process (>1 ps). The generalization of eq 2 to incorporate nonequilibrium effects is possible by changing the upper limit of the integral from infinity to t and defining a time-dependent (TD) rate constant.

The expression for $L(t)$ in eq 2 shows how the electron-transfer rate depends on the displacement $Q_{j,e} - Q_{j,CT}$ between $|D^+A^- \rangle$ and $|D^*A \rangle$ states. We approximate the surfaces of $|D^*A \rangle$ and $|D^+A^- \rangle$ states by considering the half-reactions $|D^* \rangle \rightarrow |D^+ \rangle$ and $|A \rangle \rightarrow |A^- \rangle$ independently in a four-point approximation scheme (Figure 2).^{13,21,22} In this case, we

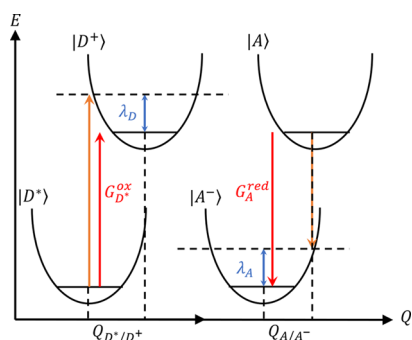


Figure 2. Schematic of the four-point approximation. Vertical transitions are shown by orange arrows. Red arrows show the oxidation- and reduction-free energy gaps, which are related to the vertical transition by the reorganization energy, shown by blue arrows. Note that the directionality of red and orange arrows represents the sign of the transition with $G_{D^*}^{ox} > 0$ and $G_A^{red} < 0$.

approximate $L(t)$ of the $|D^*A \rangle \rightarrow |D^+A^- \rangle$ reaction as the sum of an $L_D(t)$ term for the $|D^* \rangle \rightarrow |D^+ \rangle$ half-reaction and an $L_A(t)$ term for the $|A \rangle \rightarrow |A^- \rangle$ half-reaction

$$L(t) = L_D(t) + L_A(t) \quad (4)$$

where

$$L_D(t) = - \sum_j^{N_D} S_j^D [(2\bar{n}_j + 1)(1 - \cos \omega_j t) + i \sin \omega_j t] \quad (5a)$$

$$L_A(t) = - \sum_l^{N_A} S_l^A [(2\bar{n}_l + 1)(1 - \cos \omega_l t) + i \sin \omega_l t] \quad (5b)$$

Here, N_D and N_A represent the total number of normal modes of the donor and acceptor, respectively. $\{S_j^D\}$ and $\{S_l^A\}$ are the Huang–Rhys factors for the $|D^* \rangle \rightarrow |D^+ \rangle$ and $|A \rangle \rightarrow |A^- \rangle$ transitions, respectively. The imaginary parts of eqs 5a and 5b will have the effect of shifting the center of the electron-transfer lineshapes by the reorganization energy while the real part will act to dephase the electronic coherence. $g(t)$ treats the bath coupling to the overall reaction as an effective Brownian oscillator under high-temperature ($k_B T \gg \hbar \Lambda$) and strongly overdamped solvent conditions^{23–25}

$$g(t) = - \left[\left(\frac{\Delta}{\Lambda} \right)^2 (\Lambda t - 1 + e^{-\Lambda t}) + i \left(\frac{\hbar \Delta^2}{2k_B T \Lambda} \right) (1 - e^{-\Lambda t}) \right] \quad (6)$$

The parameter Λ is the modulation frequency of the solvent oscillator or the inverse timescale of solvent relaxation. Δ represents the magnitude of the solvent-coupling strength. The solvent parameter κ is defined by their ratio

$$\kappa \equiv \frac{\Lambda}{\Delta} \quad (7)$$

We assume the slow-modulation limit, realistic for a polar solute in a polar solvent, with $\kappa = 0.1$, so that the resulting lineshapes will be nearly Gaussian.²⁴ The solvent parameters can be related to the full-width at half maximum of the lineshape, Γ , by the Padé approximant

$$\Gamma = \Delta \frac{1 + 0.85\kappa + 0.88\kappa^2}{2.355 + 1.76\kappa} \quad (8)$$

The imaginary part of eq 6 is representative of the solvent reorganization energy

$$\lambda_s = \frac{\hbar^2}{2k_B T} \left(\frac{\Lambda}{\kappa} \right)^2 \quad (9)$$

while the real part of eq 6 contributes to solvent-induced dephasing of electronic coherence.

The free-energy gap ΔG is given by

$$\begin{aligned} \Delta G &= (G_D^+ + G_A^-) - (G_{D^*} + G_A) \\ &= (G_{D^*}^{ox} + G_A^{red}) \\ &= (G_D^{ox} - E_0 + G_A^{red}) \end{aligned} \quad (10)$$

which is the Rehm–Weller equation with the Coulombic solvation energy of the ions accounted for by the solvent reorganization energy in eq 6. Expressing eq 2 in terms of oxidizing and reducing half-reactions, each with independent vibronic structures, coupled to a common bath gives

$$k_{eT} = \frac{2}{\hbar^2} |V|^2 \Re \int_0^\infty dt e^{-i/\hbar(G_{D^*}^{ox} + G_A^{red})t + L_D(t) + L_A(t) + g(t)} \quad (11)$$

It is instructive at this point to consider this expression under the high-temperature approximation with bath motions folded into $L(t)$. When $k_B T \gg \hbar \omega$

$$L(t) \approx - \frac{k_B T \lambda}{\hbar^2} t^2 - \frac{i\lambda}{\hbar} t \quad (12)$$

where $\bar{n}_j \approx k_B T / \hbar \omega_j$ is used, and

$$\lambda = \sum_j S_j \hbar \omega_j + \lambda_s = \lambda_D + \lambda_A \quad (13)$$

is the reorganization energy for the electron-transfer reaction. Substituting eq 12 into eq 2 and solving the Gaussian integral analytically gives the semiclassical Marcus rate constant expression

$$k_{eT} = (2\pi/\hbar) V^2 \frac{1}{(4\pi\lambda k_B T)^{1/2}} \exp \left\{ - \frac{(\Delta G + \lambda)^2}{4\lambda k_B T} \right\} \quad (14)$$

If we consider the numerator in the exponential of eq 14, we find that the oxidation and reduction potentials will be shifted according to their respective reorganization energies.

$$\Delta G + \lambda = (G_{D^*}^{ox} + \lambda_D) + (G_A^{red} + \lambda_A) \quad (15)$$

The up- and down-shifting away from the redox potentials by the reorganization energy can be understood by the convention shown in Figure 2 where G_A^{red} is λ_A more negative than the $|A\rangle \rightarrow |A^-\rangle$ vertical transition, and G_D^{ox} is λ_D less positive than the $|D^*\rangle \rightarrow |D^+\rangle$ vertical transition. Note that the red arrows in Figure 2 correspond with the sign of each redox potential where $G_D^{\text{ox}} > 0$ and $G_A^{\text{red}} < 0$.

Equation 11 is the time-domain expression for approximating the $|D^*A\rangle \rightarrow |D^+A^-\rangle$ electron-transfer reaction, resulting from two independent oxidation and reduction half-reactions, each with their own internal reorganization energies. This expression is written for electron transfer between a single pair of donor and acceptor diabatic states. To express the electron-transfer rate for a dye-sensitized semiconductor system requires integration in energy through the density of states of the semiconductor conduction band.¹⁰ To achieve this, we rewrite eq 11 in terms of the energy-dependent electron-transfer rate $k(E)$ multiplied by the acceptor density of states $\rho(E)$,^{10,18,19,26} such that

$$k_{\text{eT}} = \int_{-\infty}^{\infty} dE k(E) \rho(E) \quad (16)$$

where

$$k(E) = \frac{2}{\hbar^2} |V|^2 \Re \int_0^{\infty} dt e^{-i/\hbar(E+G_D^{\text{ox}})t+L_D(t)+L_A(t)+g(t)} \quad (17)$$

and $\rho(E)$ is assumed to take on the known form for the normalized state density of an isotropic crystal near the band edge¹⁰

$$\rho(E) = \begin{cases} 0 & E < G_A^{\text{red}} \\ \frac{(2m_e)^{3/2}}{2\pi^2\hbar^3} \sigma_0 (E - G_A^{\text{red}})^{1/2} & E \geq G_A^{\text{red}} \end{cases} \quad (18)$$

where m_e is the effective electron mass in the semiconductor conduction band, and σ_0 is the unit cell volume. $\rho(E)$ is the particle normalized density of states for a semiconductor which extends from the band edge (because $G_A^{\text{red}} \approx E_{\text{fb}}$, the flat-band potential). The distribution in eq 17 is centered at the oxidation potential of the donor, shifted to more negative energy by λ . Equation 17 accounts for line broadening and reorganization, resulting from both oxidation and reduction half-reactions. The total electron-transfer rate is the integral of $k(E)$ in eq 17 weighted by the density of states $\rho(E)$ in eq 18. A schematic for this situation is shown in Figure 3.

The total reorganization energy for the reaction is given by the sum of internal and solvent reorganization energies

$$\lambda = \lambda_i + \lambda_s \quad (19)$$

Here, we approximate the total solvent reorganization energy λ_s with the equation

$$\lambda_s = \frac{\Delta e^2}{2} \left(\frac{1}{r_D} - \frac{1}{R} \right) \left(\frac{1}{\epsilon_{\text{op}}} - \frac{1}{\epsilon_s} \right) \quad (20)$$

derived by Marcus for a redox reaction occurring at an electrode surface.^{11,12,27} In eq 20, r_D is the effective solvation radius of the donor, and R is twice the donor–acceptor distance. ϵ_{op} and ϵ_s are the optical and static dielectric permittivities, respectively, of the solvent and Δe is the total charge transferred. The solvent reorganization energy is

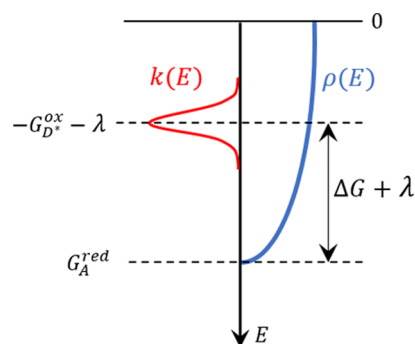


Figure 3. Schematic of the $k(E)$ and $\rho(E)$ distribution functions whose integrated overlap contributes to the electron transfer rate. In analogy with the Marcus rate expression, the energy separation between the band edge of $\rho(E)$ and the center of $k(E)$ corresponds with the free-energy gap and the total reorganization energy, $\Delta G + \lambda$.

calculated using eq 20 and is used to compute lineshape parameters in eq 9 for use in $g(t)$ in eq 6. The internal reorganization energy for donor and acceptor half-reactions is

$$\lambda_{i,D} = \sum_{i=1}^{N_D} S_i^D \hbar \omega_i \quad (21a)$$

$$\lambda_{i,A} = \sum_{i=1}^{N_A} S_i^A \hbar \omega_i \quad (21b)$$

For a total reorganization energy of

$$\lambda = \lambda_{i,D} + \lambda_{i,A} + \lambda_s \quad (22)$$

Finally, we make the Condon approximation where the electronic coupling is independent of the vibrations. Computation of the electronic coupling is described in the following section.

Electronic Coupling. A theoretical framework for extracting charge-localized basis states, their site energies, and interstate-coupling strengths has been established.^{28,29} Here, we reproduce the essential components of the work first described by Kondov et al.²⁸

To compute electron-transfer rates using eqs 16–18 requires an electronic coupling strength V . First, we extend the Hamiltonian of eq 1 to account for coupling of a donor orbital to every acceptor molecular orbital. Strictly, the coupling should be between initial and final states, $|D^*A\rangle$ and $|D^+A^-\rangle$. As an approximation, we take the $|D^*\rangle$, $|A\rangle$, donor–acceptor orbital coupling as the electron-transfer coupling with

$$|\psi_d\rangle = |D^*\rangle \quad (23a)$$

$$|\psi_a\rangle = |A\rangle \quad (23b)$$

where $|\psi_d\rangle$ is the donor molecular orbital, and $|\psi_a\rangle$ is the set of a acceptor molecular orbitals. The Hamiltonian in the prepared excited initial state in this notation is then given by

$$\hat{H} = \hat{T} + |\psi_d\rangle \hat{V}_{dd} \langle \psi_d| + \sum_a |\psi_a\rangle \hat{V}_{aa} \langle \psi_a| + \sum_a (|\psi_d\rangle \hat{V}_{da} \langle \psi_a| + |\psi_a\rangle \hat{V}_{ad} \langle \psi_d|) \quad (24)$$

where \hat{V}_{dd} and \hat{V}_{aa} are the nuclear coordinate-dependent potential energy surfaces of the donor and acceptor,

respectively. Diagonal elements V_{dd} and V_{aa} represent site energies of the donor and acceptor states, respectively. Off-diagonal elements V_{ad} and V_{da} represent the coupling strength between donor and acceptor states. In the mean-field single-electron picture, the effective Hamiltonian can be identified with the Fock (or Kohn–Sham) matrix. We choose atomic orbitals $|\varphi_j\rangle$ as the set of localized basis functions. The atomic orbitals are calculated by electronic structure methods and can be partitioned into donor and acceptor subspaces. Atomic orbitals are well localized but not orthogonal. Lowdin orthogonalization maintains the local character of the basis functions while also yielding an orthogonal basis set.³⁰ The atomic orbitals are Lowdin orthogonalized as

$$|\tilde{\varphi}_n\rangle = \sum_j (S^{-1/2})_{jn} |\varphi_j\rangle \quad (25)$$

where S is the atomic orbital overlap matrix with elements $S_{kl} = \langle \varphi_k | \varphi_l \rangle$. Similarly, the Fock matrix in the Lowdin orthogonal basis is given by

$$\tilde{F} = S^{-1/2} F S^{-1/2} \quad (26)$$

where F is the Fock matrix in the atomic orbital basis. In the donor–acceptor block structure, the orthogonalized Fock matrix is

$$\tilde{F} = \begin{pmatrix} \tilde{F}_{dd} & \tilde{F}_{da} \\ \tilde{F}_{ad} & \tilde{F}_{aa} \end{pmatrix} \quad (27)$$

With matrix elements given by

$$\tilde{F}_{\alpha\beta, nm} = \langle \tilde{\varphi}_n^\alpha | f | \tilde{\varphi}_m^\beta \rangle = \sum_i \langle \tilde{\varphi}_n^\alpha | \chi_i \rangle \epsilon_i \langle \chi_i | \tilde{\varphi}_m^\beta \rangle \quad (28)$$

where f is the Fock operator, and $|\chi_i\rangle$ is the molecular orbitals obtained from an SCF or density functional theory (DFT) calculation. α and β indices denote either donor (“d”) or acceptor (“a”) subspaces. Block diagonalization of donor and acceptor subspaces by

$$\bar{F}_{\alpha\alpha} = D_\alpha^\dagger \tilde{F}_{\alpha\alpha} D_\alpha \quad (29)$$

followed by transformation of the off-diagonal elements

$$\bar{F}_{\alpha\beta} = D_\alpha^\dagger \tilde{F}_{\alpha\beta} D_\beta \quad (30)$$

yields the block-diagonalized Fock matrix

$$\bar{F} = \begin{pmatrix} \bar{F}_{dd} & \bar{F}_{da} \\ \bar{F}_{ad} & \bar{F}_{aa} \end{pmatrix} = \begin{pmatrix} \epsilon_{d,1} & 0 & \dots & \bar{F}_{da} \\ 0 & \epsilon_{d,2} & & \\ \vdots & & \ddots & \vdots \\ \bar{F}_{ad} & \dots & \epsilon_{a,1} & 0 \\ 0 & & & \epsilon_{a,2} \end{pmatrix} \quad (31)$$

Diagonal elements of eq 31 provide the energies of localized donor and acceptor states while the off-diagonal elements provide the electronic-coupling strength between donor and acceptor states. The matrix elements can hence be identified as $\bar{F}_{da} = V_{da}$, $\bar{F}_{dd} = V_{dd}$, and $\bar{F}_{aa} = V_{aa}$. The donor and acceptor molecular orbitals are given by the eigenvectors of $\bar{F}_{\alpha\alpha}$ and are related to the atomic orbitals via

$$|\tilde{\varphi}_n^\alpha\rangle = \sum_j (D_\alpha)_{jn} |\tilde{\varphi}_j^\alpha\rangle = \sum_{j,l} (D_\alpha)_{jn} (S^{-1/2})_{lj} |\varphi_l\rangle \quad (32)$$

The off-diagonal coupling elements V_{da} are coupling strengths between a chosen donor level d and an acceptor

level a . The coupling strength V in eq 17 should be a continuous function of energy because the density of states is continuous with energy. Thus, the discrete set of coupling elements to acceptor levels calculated with the finite TiO_2 cluster needs to be converted to a form that is applicable to eq 17. To achieve this, we assume an average coupling strength taken as the average from the band edge to 0 eV. Hence, we use the finite cluster of TiO_2 to calculate the individual coupling between the dye lowest unoccupied molecular orbital (LUMO), level d , and each energy level a in the TiO_2 conduction band and then generalize to a continuous density of states by averaging the discrete couplings for incorporation into eq 17.

In summary, the electron-transfer rate can be calculated using eqs 16–18 which take Huang–Rhys factors and oxidation potentials from individual donor and acceptor units, solvent reorganization energy from eq 20, and the donor–acceptor electronic-coupling strength from the average of off-diagonal elements of eq 31.

COMPUTATIONAL DETAILS

DFT was used to investigate the electronic and structural properties of rhodamine dye chromophores bound to TiO_2 clusters. All DFT calculations were performed in the Gaussian 16 software package.³¹ TiO_2 clusters were built according to previous studies.³² Specifically, we used a $\text{Ti}_{24}\text{O}_{50}\text{H}_4$ cluster with an anatase crystal structure, and a TiO_3 fragment inserted into the center to relieve surface tension. The four hydrogen atoms saturate the dangling oxygen bonds and prevent trap states from appearing in the band gap. The cluster was minimized at the DFT/B3LYP level of theory, treating the Ti centers with a LANL2DZ effective core potential and O centers with a 3-21G basis set. Water was used as the solvent in an integral-equation-formalism polarizable continuum using the SMD model.³³ Singly deprotonated anchor-bridge groups (e.g., phenyl– PO_3H^-) were then attached to the minimized TiO_2 clusters at the [101] face, placing the hydrogen of the phosphonic anchoring group on a nearby surface oxygen atom. The entire system was then reoptimized at the same level of theory, treating all non-Ti centers with a 3-21G basis set. Following this, the xanthilium core of the dye was attached to the complex on the anchor-bridge group to build the full rhodamine dye. All atoms of the TiO_2 cluster, except the Ti center binding the dye, were then frozen for a final optimization step. For this optimization step, a PF_6^- counterion was placed in proximity to the dye, according to the crystal structure of the dye to yield a charge neutral system, consistent with experimental conditions.⁷ The geometry of the rhodamine dye and the Ti center directly attached to the phosphonate was then optimized in the presence of the frozen TiO_2 cluster.

Following geometry optimization, TD-DFT/CAM-B3LYP single-point calculations were carried out on the dye– TiO_2 complexes to yield the overlap and Kohn–Sham matrices in the S_1 Frank–Condon region. Ideally, the overlap and Kohn–Sham matrices would be calculated for the S_1 minimum geometry because Franck–Condon relaxation should occur faster than electron transfer. Because of the system size and complexity, however, these calculations are prohibitive. We, therefore, compromise by considering the S_1 electronic structure at the S_0 minimum geometry. The small Franck–Condon intensity of rhodamine dyes suggests that there will only be minimal structural reorganization from the Franck–

Condon region, which justifies this approximation. For dyes at a coplanar geometry, the dihedral angle τ was fixed while the rest of the dye was allowed to relax. TD-DFT was also used to calculate the optical transition density of the complexes, which is used to establish the donor orbital of the complex for electron-transfer calculations.

Redox potentials and reorganization energies were computed by optimizing the ground-state and first excited-state singlets, S_0 and S_1 , the lowest energy cationic doublet state, D_0 , and the lowest energy triplet state T_1 , of the dyes (B3LYP/6-311G(d)) as well as the neutral S_0 and anionic D_1 structures of the TiO_2 cluster (LANL2DZ/B3LYP/3-21G). Normal mode frequencies were computed for each dye in S_0 , S_1 , D_0 , and T_1 states and the thermally corrected free-energy differences, D_0-S_0 , were used to compute ground-state oxidation potentials, G_D^{ox} . The E_0 computed for the $S_0 \rightarrow S_1$ transition along with the ground-state oxidation potential, taken as the $S_1(\text{min})-S_0(\text{min})$ free-energy difference, was then used to compute the excited-state oxidation potential, $G_{D^*}^{ox}$, according to eq 10. The TiO_2 reduction potential, G_A^{red} , was calculated as the D_1-S_0 thermally corrected free-energy difference. Reorganization energies for each half-reaction were computed by projecting internal coordinate changes between initial and final structures onto normal coordinates, providing normal coordinate displacements which, along with normal mode frequencies, give the total internal reorganization energy. This analysis was carried out using the DUSHIN program.⁵⁴

RESULTS

Dye- TiO_2 Complex Optimized Structures. The complexes optimized using the above procedure are shown in Figure 4. The dihedral angles τ , presented in Table 1, are similar to those observed for free dyes both in DFT calculations and by X-ray crystallography.^{7,8} In particular, phenylene dyes exhibit τ angles closer to 90° , while thiophene dyes are closer to coplanarity. In contrast to previous results of

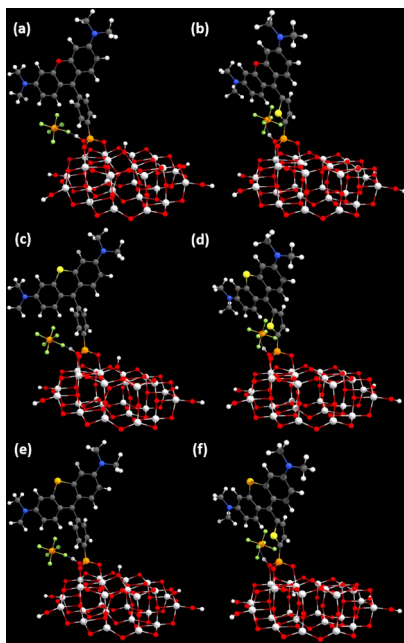


Figure 4. DFT-optimized dye- TiO_2 complexes. (a) O-Ph, (b) O-Th, (c) S-Ph, (d) S-Th, (e) Se-Ph, and (f) Se-Th.

Table 1. Comparison of Dye- TiO_2 Structures for Various Coordinates

	$1/2 R$ (Å)	τ (deg) dye- TiO_2 S_0	τ (deg) free dye S_0	τ (deg) free dye S_1	τ (deg) free dye D_0
O-Ph	8.92	84	69	52	69
S-Ph	8.92	84	90	73	84
Se-Ph	8.92	85	90	81	84
O-Th	8.60	57	66	47	69
S-Th	8.60	60	90	90	89
Se-Th	8.60	59	90	89	89

the free dyes however, there is only a small dependence of the chalcogen substitution on the observed τ angle when complexed with TiO_2 . As free dyes in solution, sulfur- and selenium-substituted analogues are found to have τ angles of nearly 90° at the ground state equilibrium geometry, whereas oxygen analogues are further away from 90° . This is because of increased rigidity along τ as the chalcogen size increased. For the complexes, we observe a similar trend but to a lesser extent. All phenylene dyes are nearly 90° , independent of chalcogen, with only a small 1° increase from 84 to 85° going from oxygen to selenium. Likewise, for thiophene, there is only a small increase in τ from 57° for oxygen to 60 and 59° for sulfur and selenium, respectively. The donor-acceptor distance, measured from the center of the xanthilium core of the dye to the surface-bonded titanium center, is presented in Table 1 and is slightly longer for X-Ph species (8.9 Å) compared to the X-Th dyes (8.6 Å) but nearly constant across the O, S, and Se series.

TD-DFT-Calculated Absorption Spectra. The lowest energy, bright $\pi-\pi^*$ transition of the free dye is a highest occupied molecular orbital (HOMO) \rightarrow LUMO transition localized on the xanthilium core. The transition energy is known to be lower for thiophene derivatives compared with phenylene. It is also known to become lower going from oxygen to sulfur to selenium.^{7,8} The dye- TiO_2 complexes also exhibit these trends as shown in Figure 5 where the lowest energy transition becomes redshifted for increasing the chalcogen size and for phenylene to thiophene substitution.

The similarity between the free dye spectra and the dye- TiO_2 complex spectra is explained by the observation that the lowest energy transition remains locally excited (LE) on the xanthilium core of the dye even when the dye is complexed with TiO_2 . This is shown for O-Ph in Figure 6. Similar results

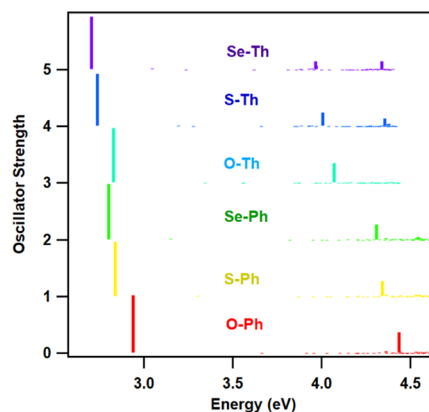


Figure 5. TD-DFT-calculated electronic absorption spectra for each dye- TiO_2 complex.

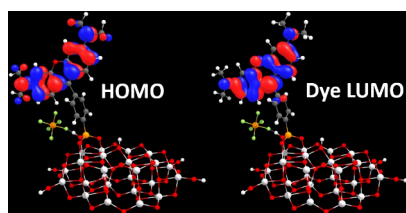


Figure 6. Plots of charge-localized molecular orbitals of the O-Ph-TiO₂ complex. The HOMO is the true HOMO of the complex while the “dye LUMO” is the LUMO of the dye manifold after block diagonalization in donor-acceptor partitioning.

are shown for each of the dyes in Figure S1. One difference however is that for thiophene compounds, the lowest energy, bright transition develops a small amount of charge transfer (CT) amplitude. This is detailed in Table 2 which lists the

Table 2. Lowest Energy Transition Properties of Each Dye-TiO₂ Complex

	transition energy (eV)	transition orbital weight	oscillator strength
O-Ph	2.94	492 → 496, 0.69 LE	1.0142
S-Ph	2.84	496 → 499, 0.69 LE	0.9675
Se-Ph	2.80	505 → 508, 0.69 LE	0.978
O-Th	2.83	493 → 498, 0.675 LE	0.9697
S-Th	2.74	493 → 499, 0.169 CT	0.9239
		497 → 501, -0.12733 CT	
Se-Th	2.71	497 → 502, 0.679 LE	0.9343
		506 → 510, -0.16 CT	
		506 → 511, 0.67 LE	

transition energy, transition orbital weights, and oscillator strengths for the lowest energy transition of each dye. While the transition is dominated by a single pair of dye-localized orbitals in phenylene compounds, thiophene compounds show a second orbital pair which is CT in character, transferring charge from the dye to TiO₂ directly. These orbitals are shown in Figure S2 and demonstrate how thiophene complexes may have a direct CT contribution to the electron-transfer process. The amplitude of the CT component is small however and we do not consider direct depopulation of the donor when calculating electron-transfer rates.

Charge-Localized Basis Analysis. The localized nature of the transition allows for treatment of the dye-TiO₂ complex in a charge-localized basis where the dye LUMO can be regarded as the donor and the manifold of TiO₂ conduction band levels as the acceptor for the purpose of calculating the electronic coupling strength V . Figure 7 shows the result of applying eqs 25–31 to the S_1 Kohn–Sham matrix of the complexes in the Franck–Condon region. The black lines are site energies of states localized on the dye while the blue lines represent site energies of states localized on the TiO₂ cluster. Each of the dye LUMO levels are positioned within the conduction band of TiO₂ but still near the band edge. This suggests that these dyes may not be well described by the “wide-band limit” picture where electronic coupling strength dominates the electron-transfer rate, while vibrations play a small role.^{15,35–37} In the wide-band limit, $k(E)$ is completely contained within the semiconductor conduction band. Thus, all vibrations of the donor can be realized, and the electron-transfer rate is temperature independent. When the distributions are not

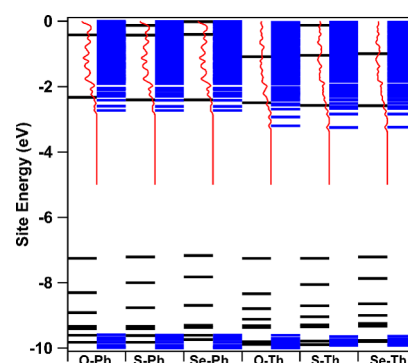


Figure 7. Donor site energies for each dye-TiO₂ complex are shown in black. Acceptor site energies are shown in blue. Red lines indicate a convolution of the TiO₂ acceptor levels with a 0.05 eV width Gaussian to help discern the distribution of levels in very dense regions where the blue lines are unclear.

totally overlapped, thermal population of vibrations and Franck–Condon factors will become important as they will affect the lineshape of $k(E)$ and thus the overlap with the density of states. This contrasts with charge-transfer complexes such as Coumarin 343 or Alizarin whose LUMO level is well within the conduction band where the wide-band limit is an adequate description.^{28,29}

The coupling strength can immediately be visualized from the differences in TiO₂ conduction bands in Figure 7. Thiophene derivatives exhibit a wider splitting of acceptor levels compared to phenylene derivatives, indicating stronger off-diagonal coupling strength.^{38,39} This is shown explicitly in Figure 8, which plots the coupling strength for each dye as a

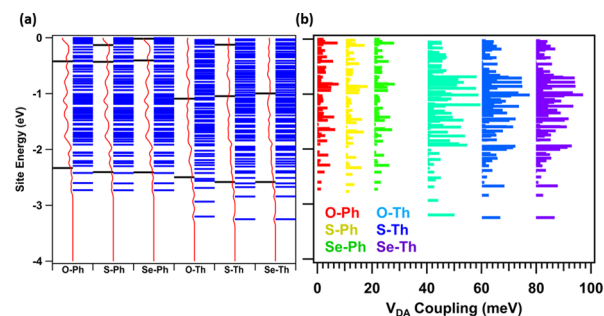


Figure 8. (a) Site energies plotted as in Figure 7 but zoomed into the -4 to 0 eV region. Red lines indicate a convolution of the TiO₂ acceptor levels with a 0.05 eV width Gaussian to help discern the distribution of levels in very dense regions where the blue lines are unclear. (b) Coupling strength between the donor orbital [lowest energy black line shown in (a)] and each acceptor state [blue lines in (a)].

function of site energy. The coupling strengths shown in Figure 8 indicate that thiophene derivatives have a more strongly coupled donor LUMO level compared to that of phenylene, which supports the enhanced splitting of acceptor levels of TiO₂ in Figure 7.

Coplanar Versus Franck–Condon Structures. Thiophene derivatives of these rhodamine dyes are known to undergo excited-state reorganization to a coplanar geometry in ~ 10 ps.⁷ This reorganization event has previously been predicted to result in much stronger coupling to an acceptor because of delocalization of the donor orbital, which would result in greater orbital overlap between the donor and

acceptor and thus stronger coupling.⁸ Here, we investigate the effect of a twisted geometry on the electronic coupling strength. Figure 9 shows a comparison of the site energies and

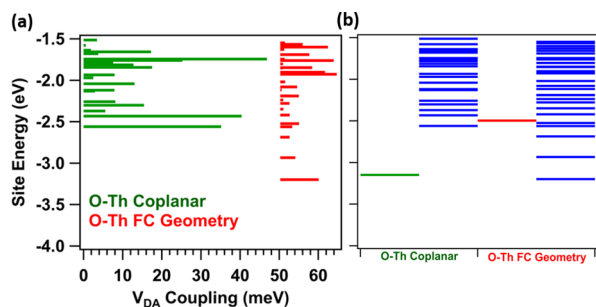


Figure 9. (a) Coupling strength as a function of acceptor site energy for coplanar O–Th (green) and O–Th at its Franck–Condon geometry (red). (b) Corresponding donor and acceptor site energies for the two structures.

coupling strengths for O–Th at the initial Franck–Condon geometry as well as at the coplanar geometry. Figure 9a shows that at coplanarity, the O–Th donor orbital is much more strongly coupled to the entire manifold of acceptor states. However, the stabilization of the LUMO at coplanarity is large enough to place the donor site energy below the conduction band edge, as shown in Figure 9b. The absence of energy resonance is why there is no widening of the acceptor levels as observed for dyes at the Franck–Condon geometry. This suggests that the forward electron-transfer rate will be reduced at a coplanar geometry, despite the large increase in electronic coupling. However, the driving force for electron transfer depends on the donor excited-state oxidation potential, acceptor reduction potential, and the reorganization energy. These parameters as well as electron-transfer rates will be presented for each complex in the following section.

Electron-Transfer Rates. The parameters calculated by DFT used to compute electron-transfer rates are shown in Table 3. Ground-state oxidation potentials match closely with experimentally determined values⁷ and show a slight shift toward less-negative $-\Delta G_D^{\text{ox}}$ values in the order O < S < Se, that is, the selenium species are slightly easier to oxidize. E_0 was determined from the free-energy difference between the S₁ and S₀ minimum geometries. X–Ph shows the expected decrease in E_0 in the order O > S > Se, consistent with the red-shift in the absorption λ_{max} with heavier chalcogen substitution. E_0 for X–Th remains nearly constant with chalcogen

substitution with a slightly higher (0.01 eV) E_0 observed for Se–Th. Although the vertical transition red-shifts with heavier chalcogen substitution for X–Th, the E_0 is sensitive to the strong π delocalization dependence on τ . O–Th has more π delocalization generated via reorganization along τ in S₁, reducing its E_0 while S–Th and Se–Th have less π delocalization in S₁ because they are more rigid about the τ coordinate but have a reduced S₁ energy because of heavier chalcogen substitution. The net E_0 results from both energy shifting by chalcogen substitution as well as τ angle changes. π delocalization is less pronounced for similar changes in τ on X–Ph, and therefore, the E_0 shift follows the shift of the vertical transition energy with chalcogen substitution. The triplet state, T₁, of Se–Th and Se–Ph has a greatly reduced E_0 in accordance with the lower energy of T₁ state relative to S₁. Likewise, O–Th at a coplanar ($\tau = 8^\circ$) geometry has a reduced E_0 consistent with previous findings.⁸

Internal reorganization energies $\lambda_{\text{I,D}}$ for the $|D^*\rangle \rightarrow |D^+\rangle$ half-reaction in Table 3 show the expected trend that the increased rigidity about the dihedral angle τ in O–Ph compared to O–Th results in lower reorganization energy. The 320 cm⁻¹ difference in reorganization energy between O–Ph and O–Th results from differences in reorganization along low-frequency torsional coordinates, which are sensitive to rigidity on τ . This can be seen in Figure 10a, which shows that the mid- and high-frequency regions (200–1700 cm⁻¹) are similar between O–Ph and O–Th while the low frequency (<200 cm⁻¹) shows a higher density of reorganization energy for O–Th. When sulfur or selenium chalcogens are substituted, the low-frequency coordinates become more rigid, and differences between phenylene and thiophene are not as pronounced. Figure 10b shows the reorganization energy distribution for the coplanar O–Th initial state. Here, the reorganization energy is much larger and dominated by low-frequency modes. T₁ initial states for Se–Th and Se–Ph show reorganization energy distributions similar to that of S₁ but with larger intensity and, for T₁ Se–Th, more low-frequency intensity. The total TiO₂ internal reorganization energy $\lambda_{\text{I,A}}$ for the $|A\rangle \rightarrow |A^-\rangle$ half-reaction is 0.63 eV, and the normal mode distribution of contributions reflects the TiO₂ vibrational density of states where the highest vibrations in the fingerprint region only extend to ~ 1200 cm⁻¹. The parameter r_d for the solvent reorganization energy is estimated as the end-to-end width along the xanthylum core of the dye while parameter R is taken from Table 1.

$k(E)$ and $\rho(E)$ distributions generated using the parameters in Table 3 are shown in Figure 11. The reorganization energy

Table 3. Redox Potentials, Reorganization Energies, Coupling Strengths and Electron-Transfer Time Constants τ_{eT} (Defined as the Inverse of k_{eT}) for Each Dye–TiO₂ Complex^a

	$-\Delta G_D^{\text{ox}}$ (eV)	E_0 (eV)	$-\Delta G_D^{\text{ox}}$ (eV)	$\lambda_{\text{I,D}}$	ΔG (eV)	$\Delta G + \lambda$ (eV)	V (meV)	τ_{eT} (ps)
O–Ph	-5.40	2.19	-3.21	0.155 eV (1248 cm ⁻¹)	-1.09	0.032	2.29	3.09
S–Ph	-5.37	2.13	-3.24	0.078 eV (626 cm ⁻¹)	-1.06	-0.079	2.13	3.60
Se–Ph	-5.36	2.10	-3.26	0.069 eV (560 cm ⁻¹)	-1.04	-0.067	2.18	3.69
O–Th	-5.41	2.07	-3.34	0.194 eV (1568 cm ⁻¹)	-0.956	0.138	5.76	0.834
S–Th	-5.40	2.07	-3.33	0.080 eV (644 cm ⁻¹)	-0.966	0.014	5.49	0.764
Se–Th	-5.38	2.08	-3.30	0.031 eV (250 cm ⁻¹)	-1.04	-0.105	5.48	0.550
O–Th coplanar		1.632	-3.75	0.67 eV (5418 cm ⁻¹)	-0.546	1.02	13.4	22.3
Se–Th triplet		1.41	-3.97	0.094 eV (756 cm ⁻¹)	-0.326	0.667	5.48	242
Se–Ph triplet		1.65	-3.71	0.071 eV (575 cm ⁻¹)	-0.586	0.385	2.18	58.2

^a $\lambda_{\text{I,A}} = 0.63$ eV, $\lambda_s = 0.28$ eV, $r_d = 11$ Å, $R = 18$ Å, $\epsilon_{\text{op}} = 1.33^2$, $\epsilon_s = 80$, $G_A^{\text{red}} = -4.296$ eV, $m_e = 9m_0$,⁴⁰ $\sigma_0 = 136$ Å³, $\kappa = 0.1$, $\Gamma = 0.27$ eV, $T = 298$ K.

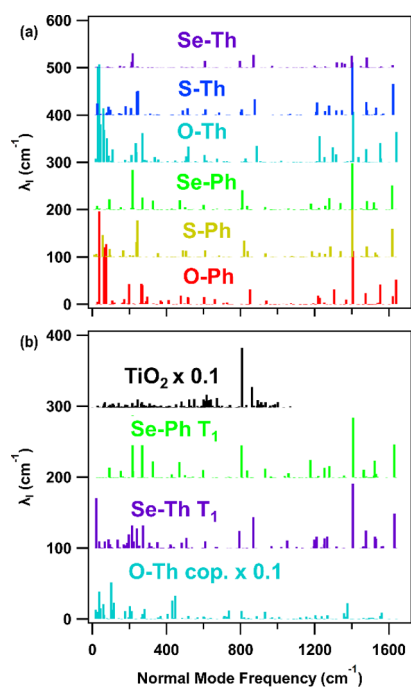


Figure 10. Reorganization energies as a function of normal mode vibrational frequency of (a) X–Ph and X–Th and (b) O–Th at the coplanar geometry and Se–Th and Se–Ph at the T_1 geometry and TiO_2 .

affects the center of $k(E)$ as well as its width. The overlap between $k(E)$ and $\rho(E)$ will thus be sensitive to $\Delta G + \lambda$ and bandwidth of $k(E)$ as they vary between each dye. Figure 11a compares X–Ph and shows, as a net result of the parameters in Table 3, nearly identical positioning of $k(E)$ independent of dye. Because the coupling strengths of each X–Ph dye are also very similar, the magnitude of $k(E)$ is similar between each X–Ph. The overall time constants for electron transfer, τ_{ET} , shown in Table 3 for each X–Ph dye are all <4 ps. X–Ph shows decreasing $-\Delta G$ in the order $\text{O} > \text{S} > \text{Se}$. Although O–Ph has the most positive excited-state oxidation potential $G_{\text{D}_2^*}^{\text{ox}}$, the large internal reorganization energy reduces $\Delta G + \lambda$, resulting in less overlap between $k(E)$ and $\rho(E)$. This is balanced by a larger coupling strength, resulting in O–Ph having the shortest

time constant (3.09 ps). S–Ph and Se–Ph have similar parameters, resulting in similar τ_{ET} of 3.60 and 3.69 ps, respectively.

Figure 11b shows the distributions for X–Th. X–Th shows decreasing $-\Delta G$ in the order $\text{Se} > \text{S} > \text{O}$. The trend is opposite to that of X–Ph because of the nearly constant E_0 across the X–Th dyes. Compounded with the decreasing internal reorganization energy in the order $\text{O} > \text{S} > \text{Se}$, the $\Delta G + \lambda$ is reduced going from O–Th to S–Th and becomes negative for Se–Th, indicating that the center of $k(E)$ for Se–Th lies slightly above the TiO_2 band edge. The coupling strengths are similar within the X–Th series, thus the electron-transfer time constant follows the trend of $\Delta G + \lambda$, producing τ_{ET} values of 0.834, 0.764, and 0.550 ps for O–Th, S–Th, and Se–Th respectively. The shorter time constants for X–Th compared to X–Ph are a result of the more than two times larger coupling strength and similar driving forces.

Figure 11c shows the distributions for T_1 states of Se–Ph and Se–Th as well as the S_1 -coplanar distribution for O–Th. The T_1 states of Se–Ph and Se–Th are assumed to have the same coupling distributions as the S_1 states of Se–Ph and Se–Th, respectively. The value of $\Delta G + \lambda$ for all three of these states is found to be significantly more positive than that of the Franck–Condon region singlet states. Thus, the electron transfer time constant is increased by one–two orders of magnitude. Although Se–Th and coplanar O–Th have similar center positions with respect to TiO_2 , the coupling strength of coplanar O–Th is up to two times larger. This is evident in the magnitude of $k(E)$ for the O–Th coplanar shown in Figure 11c. Also, because of the large internal reorganization energy of coplanar O–Th, its distribution is slightly wider. As a result, coplanar O–Th has more overlap with TiO_2 in the tail of its distribution than Se–Th. These two attributes of coplanar O–Th explain why it has a much shorter τ_{ET} than Se–Th T_1 despite having similar center positions.

DISCUSSION

Thiophene Versus Phenylene. Figure 8 shows that rhodamines with a thiophene bridge, X–Th, are more strongly coupled to TiO_2 than X–Ph. On TiO_2 , X–Th has more coplanar geometries than X–Ph, which will contribute to this higher coupling strength. Additionally, because of the electron-withdrawing nature of sulfur on the thiophene ring, thiophenes

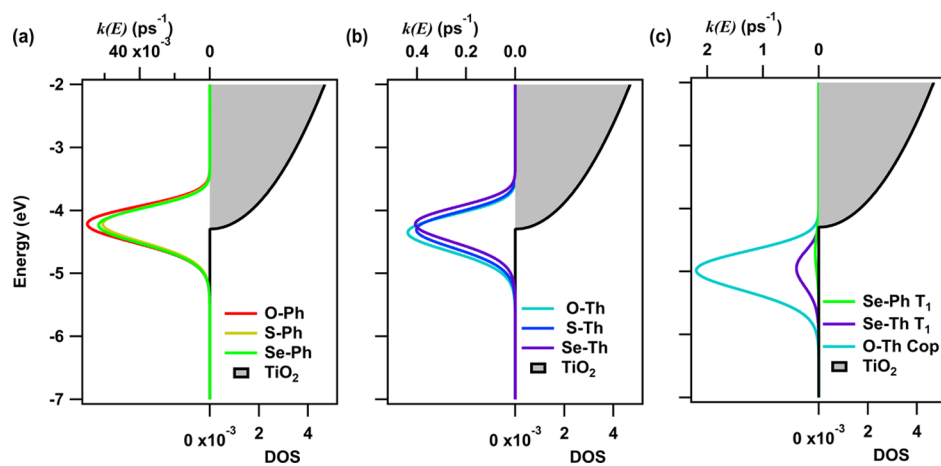


Figure 11. Dye electron distributions $k(E)$ for (a) X–Th, (b) X–Ph, and (c) triplet states of Se–Ph, Se–Th, and coplanar state of O–Th. The density of states $\rho(E)$ for TiO_2 is shown in each panel.

are known to have better charge transport properties.^{41,42} The combination of these two effects results in the enhanced orbital overlap and thus electronic-coupling strength between the X–Th donor orbital and the set of acceptor orbitals. The overall effect on the electron-transfer rate can be discerned by comparing O–Ph and O–Th. The coupling strength of O–Th is ~ 2.5 times larger than that of O–Ph. This results in a ~ 4 times shorter electron transfer rate for O–Th compared to O–Ph and shows how stronger coupling can overcome a less-favorable driving force. Comparing phenylene and thiophene bridges for sulfur-substituted dyes similarly shows increased rates for S–Th, despite a less-favorable driving force. Se–Th is shown to have the shortest electron transfer time constant because of stronger coupling when compared with Se–Ph but also because $\Delta G + \lambda < 0$. This confirms the hypothesis that X–Th is more strongly coupled to TiO₂ than X–Ph and that stronger coupling strength produces faster electron-transfer rates for dyes with similar driving forces. However, these differences are small with all dyes exhibiting < 4 ps electron-transfer time constants.

Coplanar Versus Franck–Condon Geometries. It has been shown that O–Th relaxes to a coplanar geometry ($\tau = 8^\circ$), following photoexcitation to S₁. This process occurs within 10 ps.^{7,8} It was hypothesized that at the coplanar geometry, because of extended conjugation from the xanthilium core through the aryl bridge, there should be high orbital overlap between the dye LUMO and orbitals of the TiO₂ acceptor, resulting in further enhanced electronic coupling.⁸ Figure 9a verifies this hypothesis by showing a ~ 2 times larger coupling strength for O–Th at the coplanar geometry. However, the delocalization of the LUMO results in a lowered energy of S₁ as well as a lowered S₁ oxidation potential. Furthermore, it is observed that the internal reorganization energy for the O–Th coplanar to cation geometry is very large (0.67 eV) because of the high distortion of the xanthilium core at coplanarity and a τ angle, which is far from the D₀ equilibrium value of 69°. The high reorganization energy and lowered oxidation potential combine to counteract the benefit of higher coupling strength, resulting in a slower time constant of 22.3 ps. Furthermore, the electron transfer time constant for O–Th at the Franck–Condon geometry is about a factor of 3 smaller than the time constant for twisting, which suggests that electron transfer will mostly occur from the Franck–Condon geometry.

Oxygen, Sulfur, and Selenium. Dyes X–Ph and X–Th all undergo electron transfer in < 4 ps. This is at odds with results of photocatalytic hydrogen generation experiments which show negligible activity for O–Th sensitizers, some activity for S–Th, and high activity for Se–Th.¹ This result is, however, consistent with incident photon to current efficiencies (IPCEs) for X–Th where each dye performs equally well.³ Because of higher flexibility of the aryl ring for oxygen-substituted dyes, much higher reorganization energies are observed with large contributions from low-frequency modes (Figure 10). This results in $\Delta G + \lambda$ values that are significantly less negative than ΔG for both O–Th and O–Ph, which has the effect of reducing overlap between $k(E)$ and $\rho(E)$. In contrast, sulfur and selenium dyes are more rigid, which corresponds with lower reorganization energies. These calculations predict that all dyes should perform similarly well; they all have similar oxidation potentials, the coupling strength is higher for X–Th but still appreciable for X–Ph, and the large reorganization energies for O–Ph and O–Th only

reduce their driving force by as much as ~ 80 meV, which is not enough to deactivate electron transfer relative to their large and negative ΔG . An important note is that the TiO₂ calculations presented here are highly approximate. We are modeling the bulk semiconductor flat-band potential as the reduction potential of a finite cluster in water. Thus, the position of the band-edge presented here should only be considered as the reference point for the model. The experimental flat-band potential in water is known to be around -3.86 V,⁴³ more than 0.4 V less negative than the calculated -4.296 V. More accurate calculations of the band edge and band shape are required to obtain realistic electron-transfer rates. These calculations do, however, provide an internal comparison between dyes to determine if there are any significant differences, which would set them apart in performance.

Triplet States. The high activity of Se–Th compared to O–Th and S–Th in photocatalytic hydrogen generation experiments was previously attributed to the high triplet yield of Se–Th.¹ It was proposed that the electron-transfer time constant was much larger than the S₁ lifetime of the dyes. Thus, significant electron transfer could only occur from a long-lived triplet state. This explanation for the high activity of Se–Th, however, seems to be inconsistent with both the oxidation potential of the triplet state as well as expected electron-transfer rate. As shown in Table 3, the triplet-state oxidation potentials of both Se–Ph and Se–Th are much lower than the S₁ oxidation potentials and similar to coplanar O–Th. This significantly reduces the driving force for electron transfer, which would make the presumed slow electron-transfer rate several orders of magnitude slower. Here, we indeed find that the intersystem crossing to a triplet state for Se–Ph and Se–Th significantly reduces the electron-transfer rate, which is consistent with previous studies on ruthenium complexes.⁴⁴ There is no indication, either from this study or others on rhodamine electron-transfer rates,^{9,10,45} that the electron-transfer process should have a nano to microsecond time constant and thus rely on a long-lived donor state. The local excitation of the donor is in close proximity to the acceptor and separated by only a single π -conjugated bridge unit, suggesting that the electron transfer occurs slower than strongly coupled sensitizers such as some ruthenium dyes (~ 100 fs),⁴⁴ Coumarin 343 (100–200 fs),^{28,46} Alizarin (6 fs),^{29,47,48} catechol (6 fs),⁴⁹ or perylene (20 fs)⁵⁰ but faster than sensitizers with long bridges and large donor–acceptor separation (5–10 ps).^{51,52} In some cases, even sensitizers with long spacers can exhibit sub-picosecond electron-transfer dynamics.⁵³

The discrepancy between photocatalytic hydrogen generation and ICPE results is possibly because of differences in the solvent environment as well as the aggregate structure. For simplicity, aggregation was neglected in the calculations presented here but is known to occur readily by these dyes on TiO₂ surfaces when the anchoring group is in the “para”-substituted position.^{2,3,54} It was previously shown that thiorhodamine dyes with rigid dimethylamine groups aggregate on the TiO₂ surface and undergo < 300 fs electron transfer to TiO₂.⁵⁴ However, aggregation on the TiO₂ surface opens an alternative pathway to a low-energy ion pair state where the charge is transferred from one dye to a neighboring dye in the aggregate. Because all the dyes presented here form aggregates on TiO₂, it is possible that varying accessibility of deactivating ion-pair states controls the different electron-transfer efficien-

cies. Additionally, the difference in solvent, pH, and electrolyte concentration between IPCE measurements and hydrogen generation experiments may have had a role in deciding whether deactivated states such as ion-pair and triplet states are accessed and to what degree.

CONCLUSIONS

The electron-transfer rates of a series of chalcogen-substituted rhodamine dyes, X–Ph and X–Th, bound to anatase–TiO₂ were computed by modeling the reactive potential surface in a four-point diabatic approximation scheme employing a vibronic Hamiltonian. Parameters for the model were obtained by DFT/TD-DFT calculations of the dye–TiO₂ complex as well as isolated dye and TiO₂ components. The results verify a hypothesis that thiophene-bridged dyes will be more strongly coupled to a TiO₂ acceptor, and that this stronger coupling will result in faster electron-transfer rates. When coplanarity is assumed between the π systems of the rhodamine core and bridge, stronger coupling to TiO₂ is observed; however, the driving force for electron transfer at this geometry becomes unfavorable, resulting in a slower electron-transfer time constant than at the Franck–Condon geometry. Varying the chalcogen on the dyes is found to only have a significant effect on the internal reorganization energy with little net effect on the overall electron-transfer rate. Triplet states of Se-substituted dyes are shown to have slower electron-transfer time constants because of a reduced driving force. Overall, electron transfer from each dye's S₁ donor state is predicted by these calculations to occur with a <4 ps time constant, consistent with IPCE curves, which show favorable performance independent of chalcogen substitution. These results, however, do not explain the trend observed by photocatalytic hydrogen generation that only Se–Th (X–Ph untested) has significant photocatalytic activity. More detailed models, which account for aggregation on TiO₂ as well as more accurate models for the TiO₂ acceptor and solvent environment, are needed to explore electron transfer in the experimental hydrogen production environment.

ASSOCIATED CONTENT

Supporting Information

The Supporting Information is available free of charge at <https://pubs.acs.org/doi/10.1021/acs.jpcc.9b11049>.

Molecular orbital plots for orbitals involved in electronic transitions for X–Ph and X–Th on TiO₂ (PDF)

AUTHOR INFORMATION

Corresponding Author

David W. McCamant – Department of Chemistry, University of Rochester, Rochester, New York 14627, United States;

orcid.org/0000-0002-9095-040X;

Email: david.mccamant@rochester.edu

Authors

Zachary Piontkowski – Department of Chemistry, University of Rochester, Rochester, New York 14627, United States

Yu-Chen Wang – State Key Laboratory of Physical Chemistry of Solid Surfaces, iChEM, Fujian Provincial Key Lab of Theoretical and Computational Chemistry, and College of Chemistry and Chemical Engineering, Xiamen University, Xiamen 361005, China

Yu-Xiu Liu – State Key Laboratory of Physical Chemistry of Solid Surfaces, iChEM, Fujian Provincial Key Lab of Theoretical and Computational Chemistry, and College of Chemistry and Chemical Engineering, Xiamen University, Xiamen 361005, China

Yi Zhao – State Key Laboratory of Physical Chemistry of Solid Surfaces, iChEM, Fujian Provincial Key Lab of Theoretical and Computational Chemistry, and College of Chemistry and Chemical Engineering, Xiamen University, Xiamen 361005, China; orcid.org/0000-0003-1711-4250

Complete contact information is available at: <https://pubs.acs.org/doi/10.1021/acs.jpcc.9b11049>

Notes

The authors declare no competing financial interest.

ACKNOWLEDGMENTS

The authors would like to thank Jeffrey Reimers for providing the DUSHIN code used to calculate reorganization energy distributions. This work was supported by the U.S. National Science Foundation (NSF) via Grant Numbers CHE-1566080, CHE-1834430, CHE-1900125, a Graduate Assistance in Areas of National Need (GAANN) fellowship from the U.S. Department of Education (P200A150052), and the National Science Foundation of China via grant numbers 21833006 and 21773191.

REFERENCES

- (1) Sabatini, R. P.; Eckenhoff, W. T.; Orchard, A.; Liwosz, K. R.; Detty, M. R.; Watson, D. F.; McCamant, D. W.; Eisenberg, R. From Seconds to Femtoseconds: Solar Hydrogen Production and Transient Absorption of Chalcogenorhodamine Dyes. *J. Am. Chem. Soc.* **2014**, *136*, 7740–7750.
- (2) Kryman, M. W.; Nasca, J. N.; Watson, D. F.; Detty, M. R. Selenorhodamine Dye-Sensitized Solar Cells: Influence of Structure and Surface-Anchoring Mode on Aggregation, Persistence, and Photoelectrochemical Performance. *Langmuir* **2016**, *32*, 1521–1532.
- (3) Mann, J. R.; Gannon, M. K.; Fitzgibbons, T. C.; Detty, M. R.; Watson, D. F. Optimizing the Photocurrent Efficiency of Dye-Sensitized Solar Cells through the Controlled Aggregation of Chalcogenoxanthylum Dyes on Nanocrystalline Titania Films. *J. Phys. Chem. C* **2008**, *112*, 13057–13061.
- (4) Mulhern, K. R.; Detty, M. R.; Watson, D. F. Aggregation-Induced Increase of the Quantum Yield of Electron Injection from Chalcogenorhodamine Dyes to TiO₂. *J. Phys. Chem. C* **2011**, *115*, 6010–6018.
- (5) Mulhern, K. R.; Orchard, A.; Watson, D. F.; Detty, M. R. Influence of Surface-Attachment Functionality on the Aggregation, Persistence, and Electron-Transfer Reactivity of Chalcogenorhodamine Dyes on TiO₂. *Langmuir* **2012**, *28*, 7071–7082.
- (6) Kirk, M. L.; Shultz, D. A.; Stasiw, D. E.; Lewis, G. F.; Wang, G.; Brannen, C. L.; Sommer, R. D.; Boyle, P. D. Superexchange Contributions to Distance Dependence of Electron Transfer/Transport: Exchange and Electronic Coupling in Oligo(Para-Phenylene)- and Oligo(2,5-Thiophene)-Bridged Donor–Bridge–Acceptor Biradical Complexes. *J. Am. Chem. Soc.* **2013**, *135*, 17144–17154.
- (7) Sabatini, R. P.; Mark, M. F.; Mark, D. J.; Kryman, M. W.; Hill, J. E.; Brennessel, W. W.; Detty, M. R.; Eisenberg, R.; McCamant, D. W. A Comparative Study of the Photophysics of Phenyl, Thienyl, and Chalcogen Substituted Rhodamine Dyes. *Photochem. Photobiol. Sci.* **2016**, *15*, 1417–1432.
- (8) Piontkowski, Z.; McCamant, D. W. Excited-State Planarization in Donor–Bridge Dye Sensitizers: Phenylene Versus Thiophene Bridges. *J. Am. Chem. Soc.* **2018**, *140*, 11046–11057.
- (9) Huang, J.; Stockwell, D.; Boulesbaa, A.; Guo, J.; Lian, T. Comparison of Electron Injection Dynamics from Rhodamine B to

In2O3, SnO2, and ZnO Nanocrystalline Thin Films. *J. Phys. Chem. C* **2008**, *112*, 5203–5212.

(10) Sakata, T.; Hashimoto, K.; Hiramoto, M. New Aspects of Electron Transfer on Semiconductor Surface: Dye-Sensitization System. *J. Phys. Chem.* **1990**, *94*, 3040–3045.

(11) Marcus, R. A. On the Theory of Oxidation-Reduction Reactions Involving Electron Transfer. I. *J. Chem. Phys.* **1956**, *24*, 966–978.

(12) Marcus, R. A. On the Theory of Electron-Transfer Reactions. VI. Unified Treatment for Homogeneous and Electrode Reactions. *J. Chem. Phys.* **1965**, *43*, 679–701.

(13) Chaudhuri, S.; Hedström, S.; Méndez-Hernández, D. D.; Hendrickson, H. P.; Jung, K. A.; Ho, J.; Batista, V. S. Electron Transfer Assisted by Vibronic Coupling from Multiple Modes. *J. Chem. Theory Comput.* **2017**, *13*, 6000–6009.

(14) Jortner, J.; Bixon, M. Intramolecular Vibrational Excitations Accompanying Solvent-Controlled Electron Transfer Reactions. *J. Chem. Phys.* **1988**, *88*, 167–170.

(15) Dwayne Miller, R. J.; Nozik, A. J.; Schmickler, W.; Frank, W. *Surface Electron Transfer Processes*; VCH Publishers, Inc., 1995.

(16) Todd, M. D.; Nitzan, A.; Ratner, M. A.; Hupp, J. T. Electron Transfer Rates from Time-Dependent Correlation Functions. Wave-packet Dynamics, Solvent Effects, and Applications. *J. Photochem. Photobiol., A* **1994**, *82*, 87–101.

(17) Fujihashi, Y.; Higashi, M.; Ishizaki, A. Intramolecular Vibrations Complement the Robustness of Primary Charge Separation in a Dimer Model of the Photosystem II Reaction Center. *J. Phys. Chem. Lett.* **2018**, *9*, 4921–4929.

(18) Gerischer, H. Electrochemical Techniques for the Study of Photosensitization. *Photochem. Photobiol.* **2008**, *16*, 243–260.

(19) Watson, D. F.; Meyer, G. J. Electron Injection at Dye-Sensitized Semiconductor Electrodes. *Annu. Rev. Phys. Chem.* **2005**, *56*, 119–156.

(20) Schatz, G. C.; Ratner, M. A. *Quantum Mechanics in Chemistry*; Dover: Mineola, New York, 1993.

(21) Nelsen, S. F.; Blackstock, S. C.; Kim, Y. Estimation of Inner Shell Marcus Terms for Amino Nitrogen Compounds by Molecular Orbital Calculations. *J. Am. Chem. Soc.* **1987**, *109*, 677–682.

(22) Zhang, W.; Zhu, W.; Liang, W.; Zhao, Y.; Nelsen, S. F. Ab Initio Calculations on the Intramolecular Electron Transfer Rates of a Bis(Hydrazine) Radical Cation. *J. Phys. Chem. B* **2008**, *112*, 11079–11086.

(23) Li, B.; Johnson, A. E.; Mukamel, S.; Myers, A. B. The Brownian Oscillator Model for Solvation Effects in Spontaneous Light Emission and Their Relationship to Electron Transfer. *J. Am. Chem. Soc.* **1994**, *116*, 11039–11047.

(24) Mukamel, S. *Principles of Nonlinear Optical Spectroscopy*; Oxford University Press: New York, 1995.

(25) Yan, Y. J.; Mukamel, S. Molecular Fluorescence and near Resonance Raman Yield as a Probe for Solvation Dynamics. *J. Chem. Phys.* **1987**, *86*, 6085–6107.

(26) Hopfield, J. J. Electron Transfer between Biological Molecules by Thermally Activated Tunneling. *Proc. Natl. Acad. Sci. U.S.A.* **1974**, *71*, 3640–3644.

(27) Marcus, R. A. Electrostatic Free Energy and Other Properties of States Having Nonequilibrium Polarization. I. *J. Chem. Phys.* **1956**, *24*, 979–989.

(28) Kondov, I.; Čížek, M.; Benesch, C.; Wang, H.; Thoss, M. Quantum Dynamics of Photoinduced Electron-Transfer Reactions in Dye–Semiconductor Systems: First-Principles Description and Application to Coumarin 343–TiO₂. *J. Phys. Chem. C* **2007**, *111*, 11970–11981.

(29) Li, J.; Kondov, I.; Wang, H.; Thoss, M. Theoretical Study of Photoinduced Electron-Transfer Processes in the Dye–Semiconductor System Alizarin–TiO₂. *J. Phys. Chem. C* **2010**, *114*, 18481–18493.

(30) Löwdin, P. O. On the Non-Orthogonality Problem Connected with the Use of Atomic Wave Functions in the Theory of Molecules and Crystals. *J. Phys. Chem.* **1950**, *18*, 365–375.

(31) Frisch, M. J.; Trucks, G. W.; Schlegel, H. B.; Scuseria, G. E.; Robb, M. A.; Cheeseman, J. R.; Scalmani, G.; Barone, V.; Petersson, G. A.; Nakatsuji, H.; et al. *Gaussian 16*, Revision C.01; Gaussian Inc.: Wallingford, CT, 2016.

(32) Oprea, C.; Girtu, C. I. O. M. A. Structure and Electronic Properties of TiO₂ Nanoclusters and Dye–Nanocluster Systems Appropriate to Model Hybrid Photovoltaic or Photocatalytic Applications. *Nanomaterials* **2019**, *9*, 357.

(33) Marenich, A. V.; Cramer, C. J.; Truhlar, D. G. Universal Solvation Model Based on Solute Electron Density and on a Continuum Model of the Solvent Defined by the Bulk Dielectric Constant and Atomic Surface Tensions. *J. Phys. Chem. B* **2009**, *113*, 6378–6396.

(34) Reimers, J. R. A Practical Method for the Use of Curvilinear Coordinates in Calculations of Normal-Mode-Projected Displacements and Duschinsky Rotation Matrices for Large Molecules. *J. Chem. Phys.* **2001**, *115*, 9103–9109.

(35) Ramakrishna, S.; Willig, F. Pump–Probe Spectroscopy of Ultrafast Electron Injection from the Excited State of an Anchored Chromophore to a Semiconductor Surface in UHV: A Theoretical Model. *J. Phys. Chem. B* **2000**, *104*, 68–77.

(36) Ramakrishna, S.; Willig, F.; May, V. Theory of Ultrafast Photoinduced Heterogeneous Electron Transfer: Decay of Vibrational Coherence into a Finite Electronic–Vibrational Quasicontinuum. *J. Chem. Phys.* **2001**, *115*, 2743–2756.

(37) Lanzafame, J. M.; Palese, S.; Wang, D.; Miller, R. J. D.; Muentner, A. A. Ultrafast Nonlinear Optical Studies of Surface Reaction Dynamics: Mapping the Electron Trajectory. *J. Phys. Chem.* **1994**, *98*, 11020–11033.

(38) Nilsing, M.; Persson, P.; Ojamäe, L. Anchor Group Influence on Molecule–Metal Oxide Interfaces: Periodic Hybrid DFT Study of Pyridine Bound to TiO₂ Via Carboxylic and Phosphonic Acid. *Chem. Phys. Lett.* **2005**, *415*, 375–380.

(39) Persson, P.; Lundqvist, M. J.; Ernstorfer, R.; Goddard, W. A.; Willig, F. Quantum Chemical Calculations of the Influence of Anchor-Cum-Spacer Groups on Femtosecond Electron Transfer Times in Dye-Sensitized Semiconductor Nanocrystals. *J. Chem. Theory Comput.* **2006**, *2*, 441–451.

(40) Kormann, C.; Bahnemann, D. W.; Hoffmann, M. R. Preparation and Characterization of Quantum-Size Titanium Dioxide. *J. Phys. Chem.* **1988**, *92*, 5196–5201.

(41) Gong, J.; Liang, J.; Sumathy, K. Review on Dye-Sensitized Solar Cells (DSSCs): Fundamental Concepts and Novel Materials. *Renewable Sustainable Energy Rev.* **2012**, *16*, 5848–5860.

(42) Mishra, A.; Fischer, M. K. R.; Bäuerle, P. Metal-Free Organic Dyes for Dye-Sensitized Solar Cells: From Structure: Property Relationships to Design Rules. *Angew. Chem., Int. Ed.* **2009**, *48*, 2474–2499.

(43) Rothenberger, G.; Fitzmaurice, D.; Graetzel, M. Spectroscopy of Conduction Band Electrons in Transparent Metal Oxide Semiconductor Films: Optical Determination of the Flatband Potential of Colloidal Titanium Dioxide Films. *J. Phys. Chem.* **1992**, *96*, 5983–5986.

(44) Asbury, J. B.; Anderson, N. A.; Hao, E.; Ai, X.; Lian, T. Parameters Affecting Electron Injection Dynamics from Ruthenium Dyes to Titanium Dioxide Nanocrystalline Thin Film. *J. Phys. Chem. B* **2003**, *107*, 7376–7386.

(45) Hilgendorff, M.; Sundström, V. Dynamics of Electron Injection and Recombination of Dye-Sensitized TiO₂ Particles. *J. Phys. Chem. B* **1998**, *102*, 10505–10514.

(46) Rehm, J. M.; McLendon, G. L.; Nagasawa, Y.; Yoshihara, K.; Moser, J.; Grätzel, M. Femtosecond Electron-Transfer Dynamics at a Sensitizing Dye–Semiconductor (TiO₂) Interface. *J. Phys. Chem.* **1996**, *100*, 9577–9578.

(47) Duncan, W. R.; Stier, W. M.; Prezhdo, O. V. Ab Initio Nonadiabatic Molecular Dynamics of the Ultrafast Electron Injection across the Alizarin–TiO₂ Interface. *J. Am. Chem. Soc.* **2005**, *127*, 7941–7951.

(48) Huber, R.; Moser, J.-E.; Grätzel, M.; Wachtveitl, J. Real-Time Observation of Photoinduced Adiabatic Electron Transfer in Strongly Coupled Dye/Semiconductor Colloidal Systems with a 6 fs Time Constant. *J. Phys. Chem. B* **2002**, *106*, 6494–6499.

(49) Rego, L. G. C.; Batista, V. S. Quantum Dynamics Simulations of Interfacial Electron Transfer in Sensitized TiO₂ Semiconductors. *J. Am. Chem. Soc.* **2003**, *125*, 7989–7997.

(50) Oliboni, R. S.; Yan, H.; Fan, H.; Abraham, B.; Avenoso, J. P.; Galoppini, E.; Batista, V. S.; Gundlach, L.; Rego, L. G. C. Vibronic Effects in the Ultrafast Interfacial Electron Transfer of Perylene-Sensitized TiO₂ Surfaces. *J. Phys. Chem. C* **2019**, *123*, 12599–12607.

(51) Asbury, J. B.; Hao, E.; Wang, Y.; Lian, T. Bridge Length-Dependent Ultrafast Electron Transfer from Re Polypyridyl Complexes to Nanocrystalline TiO₂ Thin Films Studied by Femtosecond Infrared Spectroscopy. *J. Phys. Chem. B* **2000**, *104*, 11957–11964.

(52) Wenger, B.; Bauer, C.; Nazeeruddin, M. K.; Comte, P.; Zakeeruddin, S. M.; Grätzel, M.; Moser, J.-E., Electron Donor-Acceptor Distance Dependence of the Dynamics of Light-Induced Interfacial Charge Transfer in the Dye-Sensitization of Nanocrystalline Oxide Semiconductors. *SPIE*, 2006; Vol. 6325.

(53) Piotrowiak, P.; Galoppini, E.; Wei, Q.; Meyer, G. J.; Wiewiór, P. Subpicosecond Photoinduced Charge Injection from “Molecular Tripods” into Mesoporous TiO₂ over the Distance of 24 Angstroms. *J. Am. Chem. Soc.* **2003**, *125*, 5278–5279.

(54) Mark, M. F.; Kryman, M. W.; Detty, M. R.; McCamant, D. W. Intermolecular Charge Separation in Aggregated Rhodamine Dyes Used in Solar Hydrogen Production. *J. Phys. Chem. C* **2018**, *122*, 16519–16531.